ICAS 2021 SHANGHAI
International Council of the Aeronautical Sciences
32nd Congress of the International Council of the Aeronautical Sciences
September 6-10, 2021
Pudong Shangri-La, Shanghai, China

# On the assessment of CFD methods for vortical flows

Roberto Gonzalez, Simon A. Prince

Centre for Aerospace, Cranfield Univeristy, UK

## Abstract

*In this study, a general assessment was made on the capabilities of a wide range of turbulence models – both linear and non-linear eddy viscosity models, and simulation techniques to predict the process of vortex formation, growth and breakdown on a series of models at a range of Mach numbers (subsonic, transonic and supersonic) and angles of attack. The analysis was made on isolated components as a first approach to study the aerodynamics of a high-speed vehicle concept and used experimental data as the basis for a detailed validation exercise. These components included a family of slender axisymmetric bodies, a family of delta wings with different leading-edge radii and a double delta wing with different edge fillet configurations. Individual studies were made on each component, and different simulation approaches were used on each of them. It was found that the most accurate turbulence models were the k-e Realisable and k-w SST models, while the Scale Adaptive Simulation method was found to be the most accurate scale resolving turbulence approach.*

**Keywords: Vortex simulation, CFD, Delta Wings, Axisymmetric bodies.**

## 1. Introduction

High-speed aircraft configurations have often employed vortex suction for the development of high lift instead of using moveable slats and flaps. The Concorde [1] and Space Shuttle SST [2] vehicles are prime examples of the use of this method for high lift generation. Slender body vehicles such as missiles also make use of vortex suction forces during manoeuvre. Military aircraft forebodies often incorporate sharp chines which fix boundary layer separation and generate strong vortices that provide for augmented manoeuvrability. The formation of these vortices, particularly from smooth surface separation, and the subsequent evolution of the non-linear suction forces they generate, remains difficult to predict given its reliance on the accurate resolution of the effects of turbulence [3]. In this study, various turbulence models were considered, and a general assessment to predict the process of vortex formation, growth and breakdown was provided. These models include linear and non-linear eddy viscosity models as well as Delayed Detached Eddy Simulation (DDES).

Three different bodies, importantly influenced by vortices, were analysed to assess different aspects related to the simulation of vortical flows, namely:

- The accuracy to predict the location of the separation point on a single delta wing with sharp and rounded leading edges (section 4.1).
- The capabilities to model the phenomena of vortex interaction on double delta wings with different edge fillet shapes (section 4.2).
- The capabilities to model and solve vortical flows subjected to compressible phenomena on axisymmetric bodies at high speeds (section 4.3).

In each part of the analysis, experimental data was also used for validation of the tested methods. Throughout the report, the details on each study, along with their results and general conclusion will be presented. This analysis was performed on isolated components as a first approach to study the more complex features of the vortex systems formed in a conceptual high-speed airframe.

## 2. Overview of vortex flow topology

### 2.1 Flowfield on a delta wing

The analysis of a delta wing having a sharp and a blunt leading edge was chosen for the first part of the assessment. In this section, the general aspects of the flow topology for single delta wings are

presented before providing in-depth details of the study, and a general presentation of the results in section 4.1.

The flow over a delta wing at an angle of attack is strongly influenced by the large vortex systems that develop over the upper surface and form from the flow separation at the leading-edge. A detailed description of the process of vortex formation and evolution before breakdown is provided in Hummel [4], Lamourne [5], Werlé [6] and Kjelgaard [7] among others. In Figure 1, the features of a typical leading-edge vortex are presented along with the general structure of a vortex system around a sharp delta wing in Figure 2.

The features of these vortices depend mostly on the angle of attack, Mach number and leading-edge sweep angle, and in Stanbrook [8] and Miller [9] the impact of each one of them is carefully detailed. With increasing angles of attack, the vortex system keeps growing in both size and extent, further enhancing its suction and contribution to the normal force produced by the wing. This trend continues until the process of vortex breakdown begins and leads to a large-scale turbulent region that further deteriorates the lift, drag and pitching moment of the wing. In-depth reviews on the features of this phenomenon on delta wings include, amongst others, Lambourne [10], Escudier [11] and Delery[12].

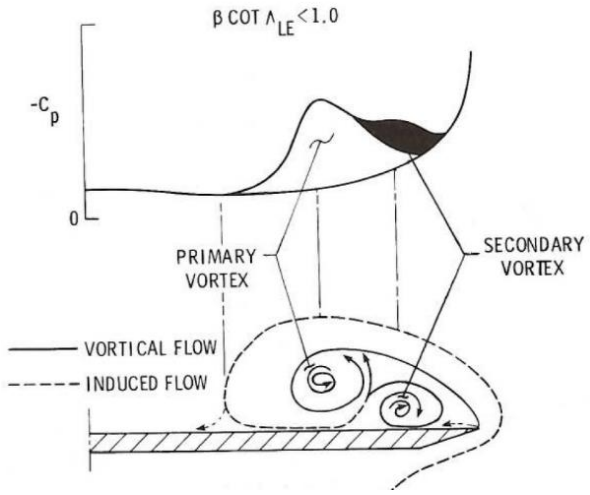


*Figure 1-Delta wing cross section. Basic features of a leading-edge vortex [9].*

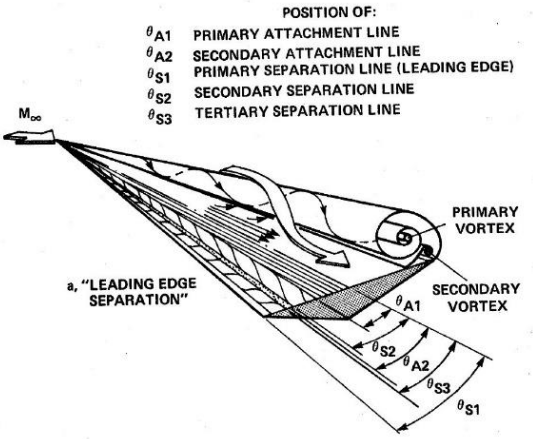


*Figure 2- Flow structure on a flat-topped delta wing with sharp leading-edge [8].*

Unlike the case of delta wings with sharp leading edges, the flow over delta wings with rounded leading-edge strongly depends on Reynolds number, given that the primary separation point is not fixed anymore. Detailed studies on the effect of leading-edge radius on this type of bodies were part of the VFE-2 study [13] which included the work of Edge, Chu and Luckring [14], Luckring [15], Coton [16] and work by Rao [17] and Kegelman[18].

The objective of this part of the study was to test the accuracy of one- and two-equation RANS turbulence models to predict the position of the primary separation point in the leading-edge region of the wings. This test is founded on the idea that a correct prediction of the primary separation point will contribute to a more accurate modelisation of the eventually fully developed vortex in this area. This will help to provide more accurate estimates of its suction pressure and flow structure, finally resulting in more reliable predictions of aerodynamic forces and moments

## 2.2 Flow topology on double-delta wings

In this section the flow topology of the body considered for the second assessment will be described before providing the details and results of this study in section 4.2. A double delta or cranked wing incorporates two different leading-edge sweep angles, the first one being the highest, usually referred to as a strake, and the second one belonging to the main wing. The mechanism of vortex formation on this type of wing is identical to the one on single delta wing. However, the evolution of the flow

topology, in this case, is more complicated given the two independent co-rotating primary vortex systems that form on each side of the wing (i.e., one coming from the strake and the other from the leading-edge kink), and dominate the flow on its upper surface as shown in Figure 3. Besides, increased vortex lift and a delayed onset of vortex breakdown are produced thanks to the energising effect of the strake vortex.

These vortices interact depending on the angle of attack and go from independent systems at low angles of attack, to a coiled system at higher incidences before the vortex breakdown point is reached. Their interaction also dependents strongly on Reynolds number effects [20]. In the experimental studies carried out by Olsen et al. [19], Verhaagen [20] and Verhaagen et al. [21], detailed descriptions of these phenomena are provided, which are part of the extensive efforts made to study the aerodynamics of this type of wing.

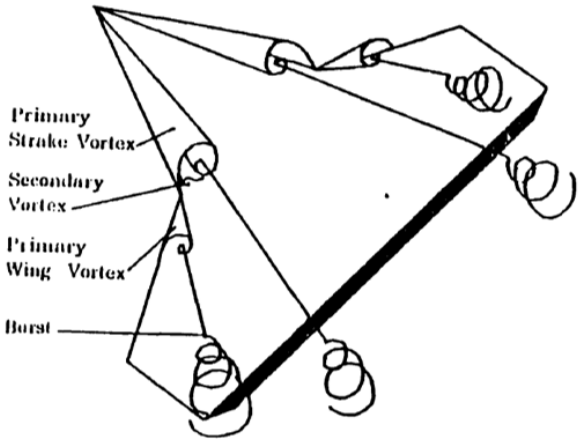


*Figure 3- Flow topology of a double delta wing [22].*

When the shape of the leading-edge kink is changed through filets, the separation patterns on the wing are modified along with the formed vortices and the way they interact. Different filet shapes were analysed in Kern [22], Erickson [23] and Hebbar [24] and studies on the effect of major wing modifications were studied by Brennenstuhl [25] and Gal [26].

The objective of this second assessment is to test the capabilities of laminar, two-, and four-equation RANS turbulence models to model the phenomena of vortex interaction present on a double delta wing with different edge fillet shapes. Accurate predictions of this phenomena would imply that the methods covered in this assessment can be applied to the study of the more complex flow topology of a complete airframe, hence the importance of this analysis.

## 2.3 Vortex flow on axisymmetric bodies

For the last part of the study a wider assessment was done on the capabilities of one-, two- and seven-equation RANS models, and high-order approximations such as Scale Adaptive Simulation (SAS) and DDES to model and solve vortical flows subjected to compressible phenomena. The analysis considered data obtained on axisymmetric bodies subjected to transonic and supersonic conditions and in this section, the general features of the vortices formed at these conditions will be presented before presenting the details of the study in section 4.3. The aerodynamic characteristics of axisymmetric bodies strongly depend on the shape and position of the separation line defined by the surface pressure distribution, which changes with incidence. With increasing angle of attack, the flow topology evolves through several distinct regimes that go from a steady symmetric system to an unsteady shedding at high angles of attack. Comprehensive descriptions of each regime are provided in Prince [3] and Rom [27]. In Figure 4, the details of a typical symmetric vortex in an axisymmetric body at subsonic speeds are presented.

The flow features are dependent on angle of attack, freestream Reynolds number, Mach number and geometric features such as fineness ratio, nose rounding and cross-section shape. The typical

documented flow structure present in transonic flow, is shown in Figure 5 and is characterised by: 1) a bow shock close to the tip of the nose, 2) expansion waves in the forebody region, 3) a crossflow shock wave that can develop, which fixes the primary separation point, and depending on the crossflow Mach number, 4) a windward shockwave extending from this embedded body shock. The latter has been found to form from the displacement effect produced by the primary vortices in the leeward region, which subsequently changes the effective geometry and the further deflection of the supersonic stream [3].

Experimental and computational studies on high-speed axisymmetric bodies are presented by Ward [28] and Prince [3] as well as by Rom [27] and Wardlaw [29] where a general description and a review are respectively presented. As mentioned, this study as a whole, represents the first approach to study the low-speed features of the vortices formed in a conceptual high-speed airframe. The results in this specific assessment, however, can be applied to the high-speed analysis of this configuration given a positive correlation.

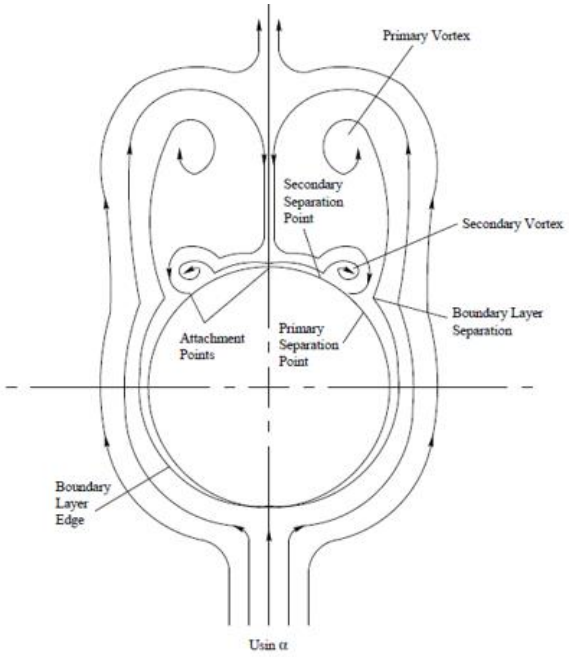


*Figure 4- Symmetric crossed-flow vortex structure [3].*

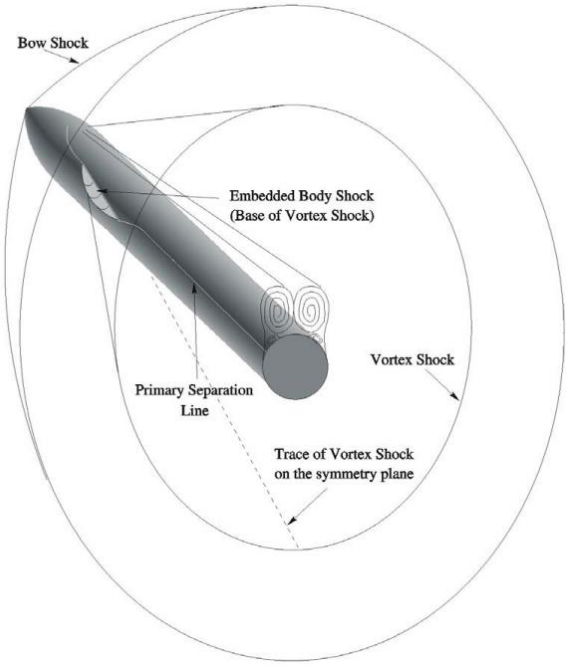


*Figure 5- Shock-wave pattern for subsonic freestream crossflow with transonic region [22].*

## 2.4 Computational Fluid Dynamics

So far, the flow topology typically encountered with the bodies analysed in this assessment has been described. In this section, a brief presentation of the methods currently available for flow simulation will be presented with a focus on vortex flows. Their respective advantages and limitations will also be included, along with comments on the selected simulation approaches for this study. The Navier-Stokes equations are a set of coupled differential equations that predict all physical flow features of an unsteady, compressible, viscous continuum flow. The idea behind Computational Fluid Dynamics relies on the mathematical manipulation of these governing equations to predict the flow properties of a specific case given a set of initial conditions, through an iterative process on a computer. This manipulation generally consists on the division of the flow domain into discrete control volumes (cells) and the integration of these governing equations along them through the use of Gauss divergence theorem as part of the Finite Volume Method [30].

Assumptions can be made to produce reduced forms of the Navier-Stokes equations that are generally less computationally expensive and faster to solve. These forms however exist at the expense of accuracy depending on the way they approximate the physical flow features. Since this

study focuses on the assessment of simulation methods to predict the steady, symmetric vortices formed at moderate angles of attack, the full Navier-Stokes equations are required to resolve the flow. The development of models for the prediction of vortex flows for general aerospace applications is still a major challenge and Luckring [31] provides a detailed chronological review on the progress up to 2019.

In Direct Numerical Simulation (DNS), the unsteady Navier-Stokes equations are numerically solved as a function of space and time, resulting in a complete description of a turbulent flow [32], [33]. The method represents the most comprehensive solution currently available. However, to accurately predict the properties of a flow, it requires a sufficiently fine mesh and sufficiently small time steps to resolve the smallest turbulent eddies and velocity fluctuations. Because of this, the method becomes so computationally demanding that its applications are generally limited to fundamental physics studies including incompressible flow and Reynolds numbers much lower than those of typical practical applications [33].

In the case of Large Eddy Simulation (LES), a spatial filtering operation is done to separate the large and small scale motions so that the full unsteady Navier-Stokes equations can be solved at length scales greater than a specific cut-off size, while the smaller turbulent scales are modelled with a sub-grid-scale (SGS) model [30]. This method requires complex algorithms to blend the resolved scales and the modelled effects smoothly, and although it can handle more complex geometries and higher Reynolds numbers than DNS, it is still computationally demanding and is used only sparingly for practical applications [33].

Another approach, focused on the mean flow properties is the Reynolds-Averaged Navier-Stokes (RANS) method where Reynolds decomposition (i.e., the definition of a property as the sum of a steady mean component and a time averaging fluctuating one) is applied to the flow velocity components and static pressure before being replaced in the Navier-Stokes equations, which are then time-averaged and solved through the use of turbulence models.

These models consider different assumptions to predict the Reynolds stresses that result from the time averaging operation, expressed as a function of eddy viscosity through the Boussinesq assumption, as well as the scalar transport terms, to close the Reynolds-Averaged Navier-Stokes equations and compute the features of turbulent flows. The models are generally classified based on the number of additional transport equations that need to be solved along with the RANS equations varying from zero in the Mixing length model to seven within the Reynolds Stress Model. In the former case, algebraic formulae for the eddy viscosity as a function of position, describe the Reynolds stresses, while in the latter, the eddy viscosity approach is avoided, and the individual components of the Reynolds stress tensor are computed directly [30].

The RANS approximation is the most widely used for practical applications due to its proven reliability and reasonable computational cost. However, given that it only produces steady solutions to the governing equations, it is not suited for the study of unsteady phenomena such as vortex breakdown. Another limitation inherent in eddy viscosity models is the inaccurate assumption of isotropic turbulence (i.e. constant fluctuations in different directions) which also reduces the accuracy of the predicted unsteady phenomena [30],[33]. Due to this statistical nature, the format of the turbulence models generally involves a combination of theoretical equations and experimentally derived calibration factors. Therefore, it is important to understand that turbulence models are only an approximation of a highly complex, unsteady flow and that the choice of turbulence model which most closely matches the flow being analysed, is the key to obtain meaningful data.

The Unsteady Reynolds-Averaged Navier-Stokes (URANS) approximation attempts to address this limitation by retaining the transient (unsteady) term in the momentum equation while using the classical RANS approximation [34],[35]. Unfortunately, preliminary computations on bodies at high angles of attack were equivalent to steady RANS simulations and did not capture any significant unsteadiness [31].

A hybrid RANS/LES approach known as Detached Eddy Simulation (DES) was developed to model the near-wall regions using a RANS approximation and to resolve the rest of the flow through an LES approximation. The model leverages some of the features of RANS and LES, which ultimately allow

for less computationally demanding unsteady simulations while achieving high levels of accuracy. The more flexible grid size requirements and the isotropic assumption of the RANS approximation allow for the modelling of the smaller eddies found inside the boundary layer (which are nearly isotropic in nature for flows at high Reynolds numbers [34]). On the other hand, the capabilities of LES properly resolve the flow regions governed by the more anisotropic larger eddies [35].

A modified distance function that depends on the local grid spacing (i.e. the maximum cell length among the three grid directions) and the wall distance is used to switch from RANS to LES modes. The function works in such a way that the RANS mode operates when the wall distance is smaller than the grid spacing, and the LES mode works outside the boundary layer where the grid spacing is smaller. This method is, however, prone to failure due to its high dependence on grid size. The use of a mesh of inadequate size, could activate the LES mode inside the boundary layer and result in a poorly resolved region and inaccurate predictions if the mesh is not fine enough for the LES approximation to resolve the small eddies present in this area [35],[36]. This switch in method due to ambiguous grid features is known as “Modelled Stress Depletion (MSD)” and represents the main limitation of the method.

The Delayed-Detached Eddy Simulation (DDES) approach is a modified version of DES that uses an adjusted switching function to “shield” the boundary layer and delay the LES mode. This function considers boundary layer information such as the kinematic eddy viscosity, the molecular viscosity and velocity gradients to blend it with any eddy viscosity model better and avoid wrong switches of approximation [36].

Another approach developed to address the MSD phenomena is known as Scale Adaptive Simulation (SAS). The method is an improved URANS formulation that relies on the use of the von Karman length scale (i.e. a parameter based on the ratio between the first and the second velocity gradients), rather than the grid spacing used in DES or the RANS turbulent length scale, to determine the local scale of the flow field. This allows the model to better detect unsteadiness and behave in a URANS manner in unsteady regions, while showing RANS capabilities in stable zones [37], [38], [39].

Altogether, this study will focus on the capability assessment of RANS and DDES approximations, given the important “cost-benefit” advantage of RANS models and the improved level of accuracy of the latter approach. In the next sections, each study will be presented along with the respective selected approximation methods.

## 3. Methodology

In the following sections, the details on the study of delta wings (section 4.1), double delta wings (section 4.2) and axisymmetric bodies (section 4.3) will be presented including the specific analysis made in each one of them, their simulation approaches and the obtained results. The experimental test cases are described in their relevant sections, along with the corresponding results and conclusions.

In each case a commercial high order Navier-Stokes solver was employed for the computations, used in either RANS mode with a suitable turbulence model, or in higher fidelity scale resolving simulation mode. In each case a second order spatial algorithm was employed with second order accuracy in time. The meshes for the study were all generated using the integrated meshing tool of ANSYS Workbench. The delta and double delta wing flows were resolved on hybrid meshes which were globally unstructured with embedded layers of prismatic cells to resolve the wall boundary layer. On the other hand the meshes for the transonic and supersonic axisymmetric body were computed using purely structured meshes and correspond to the mesh version described in Prince [3].

Since the study focused only on low to moderate angles of attack were the leeside vortex pattern was known to be steady and symmetric, each of these studies computed only half of the flow with a symmetry boundary condition imposed on the flow symmetry plane. All flow involved inclinations in the pitch plane only and no side slip cases were investigated. In each case a mesh sensitivity study was performed on the highest angle of attack case to identify the correct mesh cell density for the overall forces and moments to be mesh insensitive. The chosen mesh was then adapted in order to better resolve the vortices.

# 4. Results

## 4.1 The Single Delta Wing

### *4.1.1* Study context and mesh details

For this study, the results presented in Edge, Chu and Luckring [14] were used as the test case to validate the computational methods. Here, a 65° sweep delta-wing model having four exchangeable leading edges with different extents of leading-edge radius were tested and compared through surface pressure coefficient distribution and aerodynamic forces and moments to determine the influence of Reynolds number, Mach number and leading-edge bluntness on the general vortex flow topology.

The simulations in this section were based on the tests made at angles of attack of 7.3°, 8.3°, 9.3° and 10.3°, a Mach of 0.4 and a Reynolds number of $6x10^6$ based on mean aerodynamic chord and considered only the sharpest and bluntest leading edges. For the experiments, no transition strip was applied to the models to allow a natural boundary layer transition. CAD models of these configurations were generated based on the polynomial description provided in the study, however, rather than modelling the tapered extension of the sting used in the tests, a fairing was added to simplify the geometry, reduce the adverse influence of that extension on the flow and avoid the use of data correction methods to account for this effect. The meshes used in this section had a cylindrical flow domain with a length equivalent to 10 mean aerodynamic chords upstream, a radius of 10 mean aerodynamic chords and a length of 15 mean aerodynamic chords downstream of the wing. A total of 20 layers of hexahedral elements with an average growth ratio of 1.2 were to cover a normal distance from the surface of the model equivalent to $y^+ \approx 5$. At the end of this process, hybrid meshes composed of about $1.4x10^6$ elements were selected from a respective grid convergence study. Cut plane views showing the inflation layers on different leading-edge configurations are shown in Figure 6.

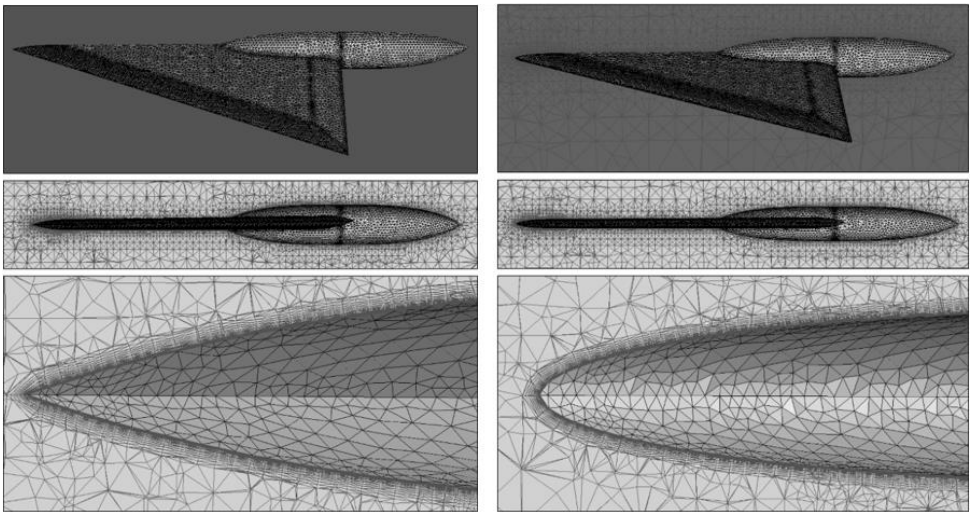

*Figure 6-Mesh for sharp (left) and large radius r/c=0.3 (right) delta wings. Detail on boundary layer treatment.*

In the analysis made in this section, a comparison between one and two-equation RANS turbulence models was made to assess their capabilities to predict the location of the separation point. This corresponds to the Spalart-Allmaras and k-ω SST turbulence models, selected based on evidence in the literature proposing them as the most accurate and efficient RANS models for vortex flow modelling [30].

### *4.1.2* Simulation details

A density-based solver was used for the steady simulations in this study since the freestream Mach numbers were high enough for this to be essential. These simulations considered a standard-type of initialisation and were solved using an implicit formulation. A Least Squares Cell-Based spatial discretisation was defined along with second-order equations for the turbulent quantities. In Table 1 more details on the chosen solution methods are provided.

| | |
|---|---|
| **Density-based formulation** | Implicit |
| **Spatial discretisation – Gradient** | Least squares cell based |
| **Spatial discretisation – Flux type** | Roe-FDS |
| **Spatial discretisation – Flow (AMG.C)** | Second order upwind |
| **Spatial discretisation - TKE** | Second order upwind |
| **Spatial discretisation – TDR** | Second order upwind |

*Table 1-Solution methods for the delta wing cases.*

A mesh adaption based on static pressure gradients was also applied to increase the accuracy of the results. This adaption was made after 2000 iterations before continuing the simulation for 5000 extra iterations.

### *4.1.3* Results

In this section, measurements of aerodynamic forces and moments, as well as pressure coefficient distribution on the upper surface of the wing, are compared against the respective simulation results.

Surface pressure measurements were obtained through series of pressure tapings placed on the upper surface of the right side at five different longitudinal stations expressed as a fraction of root chord length starting from the wing apex (i.e., $x/c_r$=0.2, 0.4, 0.6, 0.8 and 0.95).

In this comparison, however, only the results obtained in the first three stages will be presented to discard the obstruction effects produced by the fairing at the back of the model. Also, the plots shown in Figure 7 and Figure 8 only show the results obtained at 10.3° given the greater influence vortices exert at this angle.

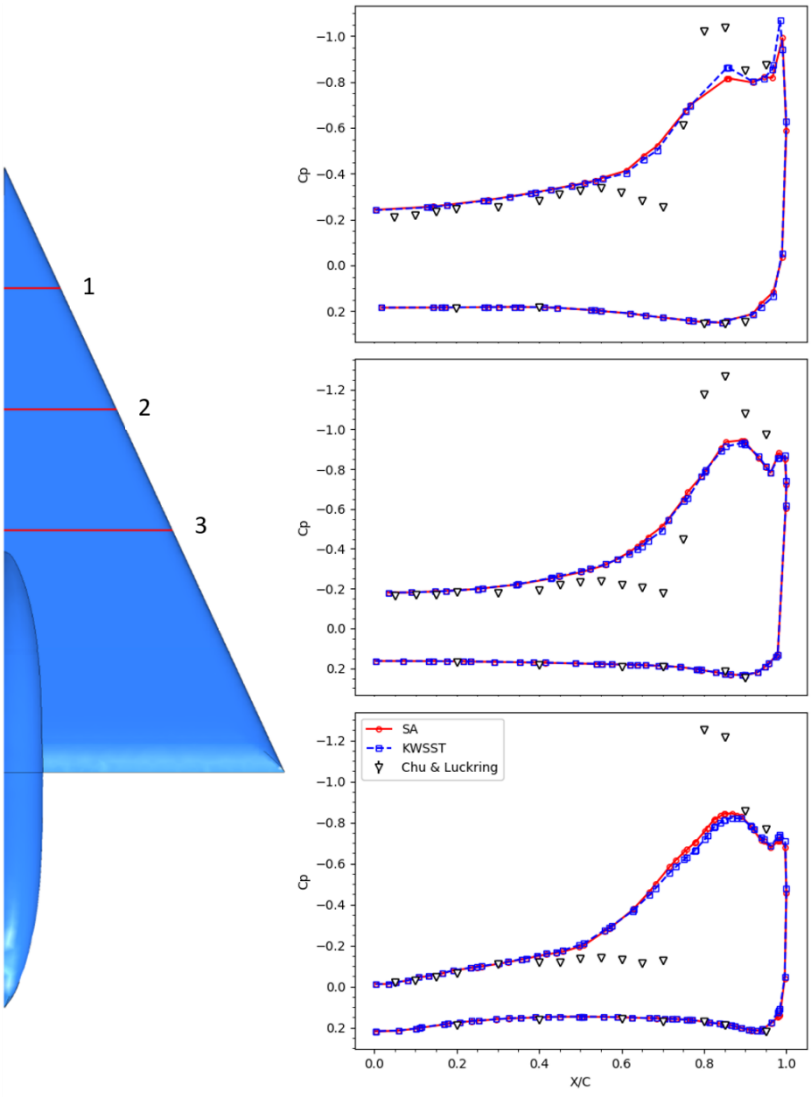

*Figure 7- Cp distribution for sharp leading-edge wing. M=0.4, $Re_c$=6x10$^6$, α = 10.3$^o$. Stations 1-3 from top to bottom.*

Plots comparing the results of normal force and pitching moment coefficients are presented for all the tested angles of attack in figure 9 and 10 for the sharp and rounded cases respectively. Here only the two-equation k-ω-SST model results are plotted against experiment, as those obtained from the Spalart Almaras model were almost identical. In this case, the reference point for the moment measured in the experiments was located at two-thirds of the root chord aft of the wing apex.

While the forces and moments for the sharp delta wing were found to agree relatively well with experiment, only normal force coefficient trends were found to be well predicted for the rounded leading-edge case. The discrepancy in the comparison of pitching moment may well be associated with the existence of significant region of laminar separation and subsequent vortex formation at the apex of the model in the untripped experimental case.

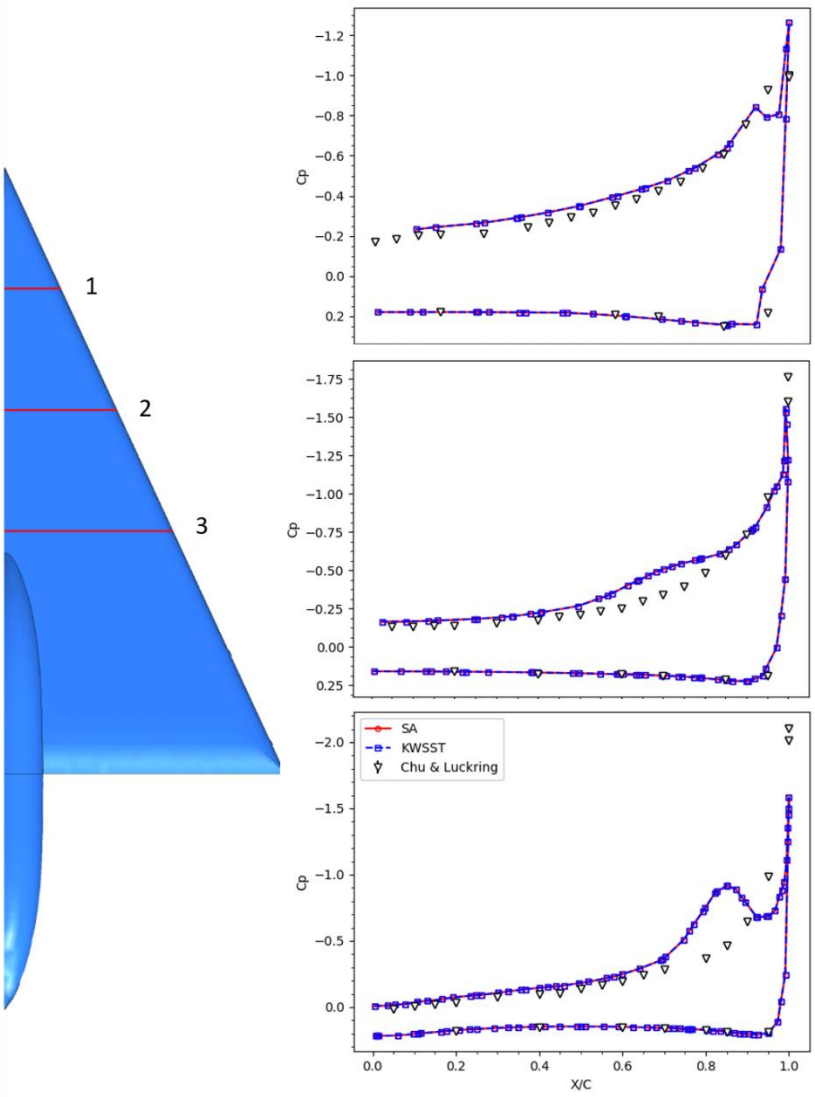


*Figure 8- Cp distribution for large leading edge radius wing. M=0.4, $Re_c$=6x10$^6$, α = 10.3$^o$.Stations 1-3 from top to bottom.*

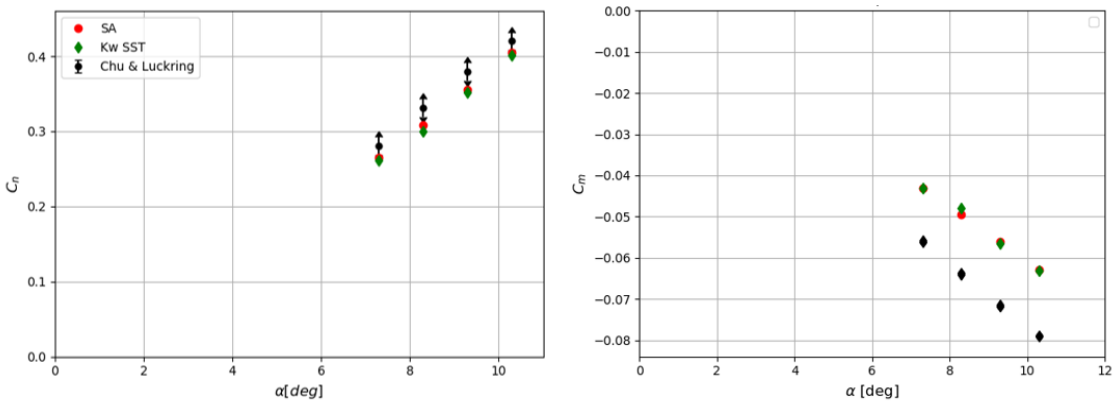


*Figure 9- Aerodynamic forces and moments vs angle of attack. Results for sharp model, M=0.4, $Re_c$=6x10⁶.*

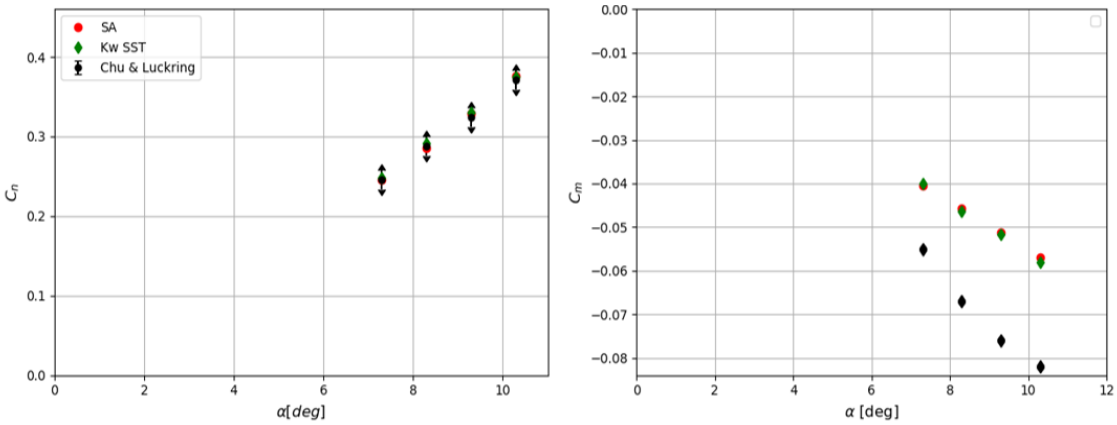


*Figure 10-Aerodynamic forces and moments vs angle of attack. Results for rounded leading-edge model. M=0.4, $Re_c$=6x10⁶.*

Although the surface pressure predictions for the case with rounded leading-edge showed good agreement with the experimental data both quantitatively and qualitatively, except in the resolution of vortex suction at the rearmost station, the results for the sharp-edged case considerably underpredict the sharpness of the rise in vortex suction, and the peak suction magnitude.

The experimental model was smooth surfaced with no boundary layer tripping. There would have been small but significant regions of laminar flow near the apex of the delta wings resulting in early laminar type vortex formation, and subsequently stronger vortices at downstream stations than would be expected from a fully turbulent boundary layer from the apex. This may explain the differences between the predicted (fully turbulent everywhere) and measured vortex suctions. In the rounded leading-edge case, the strong surface curvatures at the nose apex may have led to earlier boundary layer transition on the lower surface than seen in the sharp-edged case, where a much greater extent of laminar separation occurred. Simulations considering high-order approximations, i.e., zonal laminar/DDES, are planned to be made to test this hypothesis as part of the next stage of this study.

## 4.2 The Double Delta Wing

### *4.2.1* Study context and mesh details.

The same kind of capability assessment was done on double-delta wings in subsonic flow conditions. For this analysis, the data from Erickson and Gonzalez [23] was taken as reference for comparison. Here, the flow topology over a series of double delta wings having different edge fillet configurations at the joint region between the main wing and the strake was analysed and compared through pressure-sensitive paint (PSP) and electronically-scanned pressure (ESP) techniques.

For this study, the three analysed fillet configurations in Erickson and Gonzalez [23] were considered: i.e. baseline (sharp transition), diamond and parabolic. The simulations were made for the Mach 0.5 condition (Reynolds number of 2x10$^6$ based on root chord length) at an angle of attack of 10° and

were done on hybrid meshes. These were composed of about $1.8x10^6$ elements and were respectively chosen from an individual grid convergence study given the geometric differences and the inherent vortex pattern of each fillet configuration. The flow domain extended for 12 and 8 characteristic lengths (wing root chord) downstream and upstream of the wing respectively. A total of 18 layers of hexahedral elements with an average growth ratio of 1.2 were applied to the surface mesh of the model such that the wall $y^+$ was no more than 5.

In the assessment done in this part of the study, a comparison between laminar, the $k$-$\omega$ SST two-equation RANS turbulence model, and a transition model (Transition-SST) [40] was made. The choice of the four-equation Transition-SST model was made to see if it could provide better Cp predictions in the wing apex region where, in the absence of effective boundary layer tripping, the early vortex formation may be of a laminar type prior to transition further downstream. On the other hand $k$-$\omega$ SST was chosen considering the results obtained in section 4.1 and as explained in Versteeg [30], the fact that out of the two-equation RANS turbulence models, it is the best suited for cases with flow separation.

### *4.2.2* Simulation details

A density-based solver was used for the steady simulations in this study considering the presence of compressibility effects at the experimental conditions. These simulations considered a hybrid-type of initialisation and were solved using an implicit formulation. A least Squares Cell-Based spatial discretisation was defined along with first-order equations for the turbulent quantities to reduce computational cost. In Table 2, more details on the chosen solution methods are provided.

| | |
|---|---|
| **Density-based formulation** | Implicit |
| **Spatial discretisation - Gradient** | Least squares cell based |
| **Spatial discretisation – Flux type** | Roe-FDS |
| **Spatial discretisation – Flow (AMG.C)** | Second order upwind |
| **Spatial discretisation - TKE** | First order upwind |
| **Spatial discretisation – TDR** | First order upwind |

*Table 2-Solution methods for the double delta wing study.*

A mesh adaption based on static pressure gradients was also applied per fillet configuration to increase the accuracy of the results. This adaption was made after 3000 iterations before continuing the simulation resulting in a total of 9000 iterations per case.

### *4.2.3* Results

In this section, results of pressure coefficient distribution on the upper surface is presented in terms of plots and contours. The plots shown in Figure 11, Figure 12 and Figure 13, compare the computational results for the baseline, diamond and parabolic fillets against their respective experimental data measured at three different longitudinal positions expressed as a percentage of root chord from the wing apex: i.e. 25%, 75% and 90%.

The contours include the computational pressure coefficient distribution compared against the respective experimental pressure-sensitive paint image. The scaling for the simulation contours was set to be as close as possible to the experimental criteria. In both cases, regions of higher suction pressure are marked by blue and purple colours, whereas the lower suction zones are denoted mainly by yellow and red colours. A comparison of aerodynamic forces and moments is also presented in Table 3, Table 4 andTable 5. The reference point for the pitching moment measured in the experiments was located at 0.2977m aft of the wing apex.

| Model | $C_L$ | $C_{L(EXP)}$ | % Error | $C_D$ | $C_{D(EXP)}$ | % Error | $C_M$ | $C_{M(EXP)}$ | % Error |
|---|---|---|---|---|---|---|---|---|---|
| Laminar | 0.3594 | 0.4 | 10.14 | 0.1051 | 0.1125 | 6.52 | 0.073 | 0.06 | 21.8 |
| Kw-SST | 0.3542 | | 11.43 | 0.1056 | | 6.11 | 0.064 | | 8.02 |
| Transition-SST | 0.3796 | | 5.08 | 0.1069 | | 4.9 | 0.064 | | 7.71 |

*Table 3-Aerodynamic forces and moments, double delta wing with baseline fillet. M=0.5, $Re_c$=2x10$^6$, $\alpha$ = 10$^o$.*

Based on Figure 11 it can be seen that the strake and wing vortices are resolved by the different methods and the results give a reasonable prediction of their position along the wing when compared

to the experimental data. This includes the prediction of the higher induced suction produced by the wing vortex at x/c=75% and the comparable suction magnitude of both vortex systems at x/c=90%. The laminar prediction is clearly inaccurate compared with the experiments. The turbulent CFD methods correctly captured the presence of two separate vortices from the two wing sections, although the inner vortex emanating from the strake section is seen to dissipate in the computationally resolved flow, earlier than is seen in the experimental image. Looking at the surface Cp versus y/c comparisons at the three measurement planes, it can be seen that while the two turbulent solutions captured both the suction peaks at about the right location, and the general trends in the pressure distribution, the magnitude of these vortex suctions do not compare well with the experimentally measured values. At the most upstream measurement plane on the strake, the steep pressure recovery seen in the experimental measurement is not properly resolved in the CFD distributions. If anything the laminar solution seems to better resolve this recovery. This is what one would expect if, as was suggested earlier, the flow close to the apex of the wing, on the forward strake in the absence of boundary layer tripping, is actually laminar. Although the Transition SST model provides more accurate force and moment predictions than the *k-ω* SST model (table 3), the only noticeable improvement in the Cp comparisons is seen towards the rear of the wing where it better predicts the outboard (main wing) vortex suction.

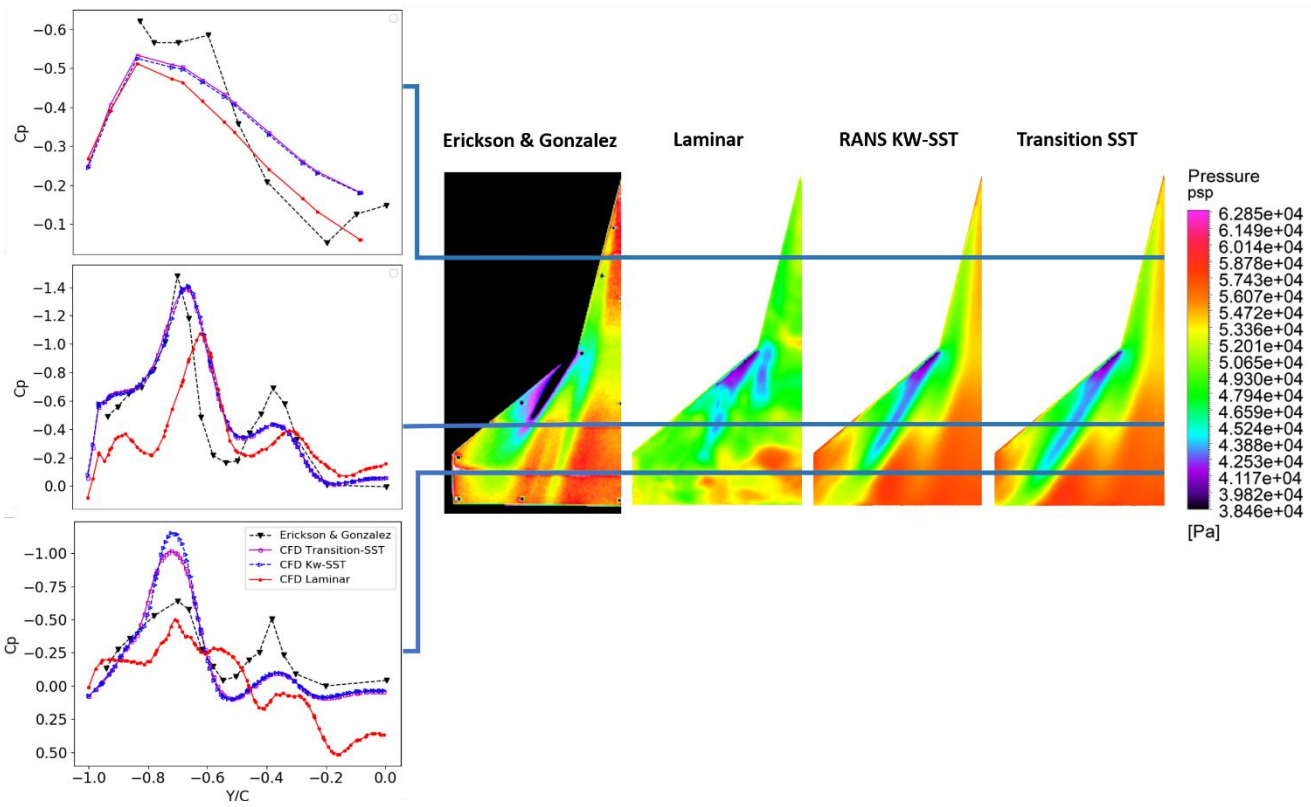


*Figure 11-Double Delta with baseline fillet, experimental PSP versus CFD resolved surface Cp distribution. M=0.5, $Re_c$=2x10⁶, $\alpha$ = 10°.*

The diamond fillet configuration was developed to produce extra lift by promoting the formation of multiple vortex systems from the additional leading-edge discontinuities it introduces at the wing-strake intersection. In Erickson [23], it was suggested from the signatures revealed by the PSP picture taken at this condition, that five co-rotating vortices were formed: i.e. one from the strake, two from the fillet and two along the wing and the interaction between the systems further downstream generates the suction peaks measured on the model at x/c=75% and 90%. This is shown in Figure 12, along with the respective computational results. Again, the laminar CFD result is clearly inaccurate for this Reynolds number over most of the wing. Interestingly both laminar and turbulent results at the strake measurement station are very close, and both significantly underpredict the outboard suction

(by nearly a half), so the effect of laminar flow here does not seem to explain the difference between CFD and experiment. In general the flow structure resolved by the turbulence models agrees with that measured in experiment. The suction peaks from the two main vortices are resolved in the right spanwise positions, but the magnitudes of these peak suctions on the intermediate plane is considerably underpredicted. Again, there is not a big discrepancy between the fully turbulent results and the ones obtained using the Transition SST model, with only subtle differences in the resolution of the peak suction magnitude (Transition SST being closer to experiment). Table 4 presents the comparison of the overall forces and moments and shows that, contrary to expectation, the *k-ω* SST model provides considerably more accurate predictions for all three components, than the Transition SST model, being within 7% of the measured result.

| Model | $C_L$ | $C_{L(EXP)}$ | % Error | $C_D$ | $C_{D(EXP)}$ | % Error | $C_M$ | $C_{M(EXP)}$ | % Error |
|---|---|---|---|---|---|---|---|---|---|
| Laminar | 0.4077 | 0.44 | 7.33 | 0.1098 | 0.124 | 11.39 | 0.075 | 0.065 | 17.39 |
| Kw-SST | 0.4101 | | 6.79 | 0.1144 | | 7.71 | 0.066 | | 4.23 |
| Transition-SST | 0.3903 | | 11.29 | 0.1094 | | 11.74 | 0.068 | | 7.75 |

*Table 4-Aerodynamic forces and moments, double delta wing with diamond fillet. M=0.5, $Re_c$=2x10⁶, $\alpha$ = 10º.*

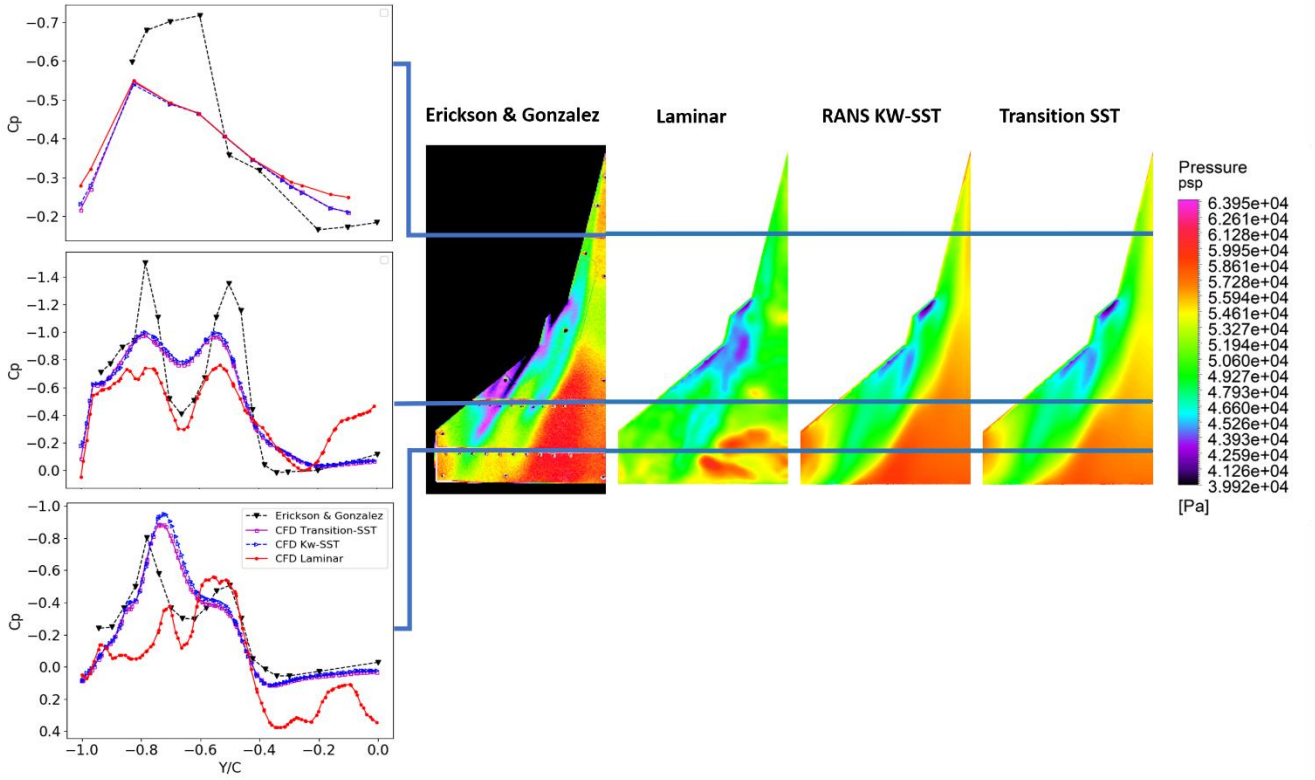


*Figure 12-Double Delta wing with diamond fillet, experimental PSP versus CFD resolved Cp distribution. M=0.5, $Re_c$=2x10⁶, $\alpha$ = 10º.*

The parabolic fillet was designed to promote a single, more stable vortex system above the wing and in fact from the PSP picture shown in Figure 13 the pressure signature of a unique dominant vortex system is observed along the whole leading edge of the wing. This experimental result, is also successfully predicted by the computational solutions, including the one laminar model where a similar flow topology is obtained to some extent.

The solutions for the *k-ω* SST model and the Transition SST model do not appear to be significantly different, suggesting that any initial laminar flow at the apex of the strake section does not affect the downstream flow much. Here, again, the strong pressure recovery inboard of the strake vortex suction is not captured by the CFD methods. While the single strong vortex suction seen in the experimental measurements is resolved in the correct spanwise position, the associated suction magnitude is not well resolved by the turbulent CFD methods. The *k-ω* SST model more accurately predicts the overall force and moment characteristics (to within 8.5% of the measured values) compared with the transition SST model. This suggests that the hypothesis that the overall flow structure, and the forces and

moments may be sensitive to laminar flow on the strake is probably not correct.

| Model | CL | $CL_{EXP}$ | % Error | CD | $CD_{EXP}$ | % Error | CM | $CM_{EXP}$ | % Error |
|---|---|---|---|---|---|---|---|---|---|
| Laminar | 0.4021 | | 12.56 | 0.1069 | | 14.45 | 0.077 | | 20.9 |
| Kw-SST | 0.4222 | 0.46 | 8.21 | 0.1144 | 0.125 | 8.41 | 0.064 | 0.064 | 0.062 |
| Transition-SST | 0.4095 | | 10.96 | 0.1102 | | 11.78 | 0.065 | | 2.26 |

*Table 5 - Aerodynamic forces and moments, double delta wing with parabolic fillet M=0.5, $Re_c$=2x10⁶, $\alpha$ = 10º.*

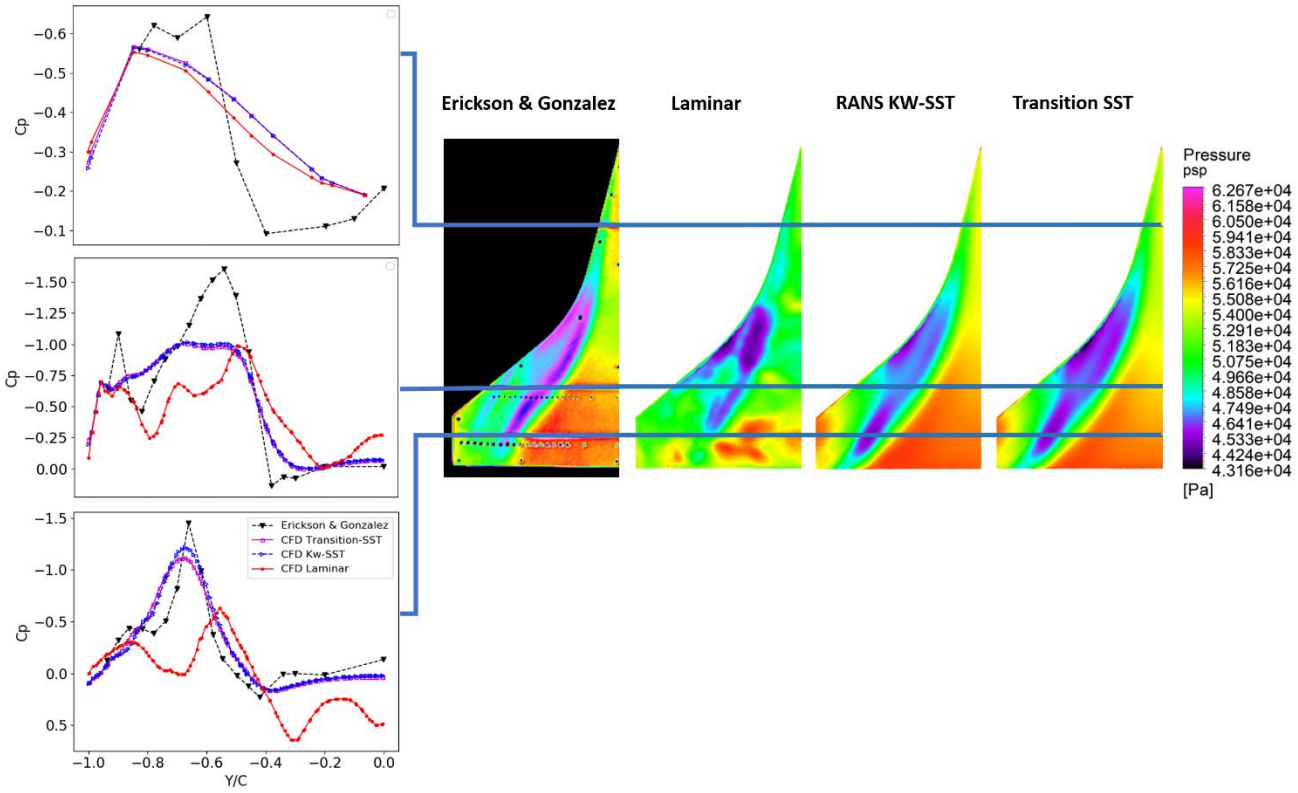


*Figure 13-Double delta wing with parabolic fillet, experimental PSP versus surface Cp distribution. M=0.5, $Re_c$=2x10⁶, $\alpha$ = 10º.*

In general the CFD methods predicted that the parabolic edge fillet produced higher vortex-induced suction peaks at x/c=0.75 and 0.90 and an overall higher lift coefficient when compared to the other fillet configurations. Calculations on the diamond fillet also showed an overall increase in the vortex-induced suction pressure levels at the downstream positions and a consequent increase in the aerodynamic forces when compared against the baseline configuration. This increase, however, was not as pronounced as the one produced by the parabolic fillet. These trends are in clear agreement with the ones identified in Erickson & Gonzalez [23].

## 4.3 The Axisymmetric Forebody Studies

### *4.3.1* Study context and mesh details

The data obtained so far has allowed the determination of adequate methods for the calculation of the vortical flow over low aspect ratio wings. However, to achieve a reliable analysis of a fully integrated airframe at full-scale and allow further design improvements, assessments of the vortical flow around isolated fuselage bodies or forebodies is also required. In this section, an extension of the work made by Prince [3] on axisymmetric bodies (missile-shaped forebodies) is presented.

A full turbulence model comparison was made including one-, two- and seven-equation RANS models and high-order approximations such as Scale Adaptive Simulation (SAS) and Delayed Detached Eddy Simulation (DDES). This study was focused on only the RAE B1A [28] forebody configuration. This body consisted of a 3-calibre ogive nose attached to a 10-calibre cylindrical section and had a body

diameter of 93.98mm. For this series of experiments, a transition strip of carborundum grit of height 0.5mm was attached at x/D=0.3 for a fully turbulent boundary layer further downstream. Cases 5 and 8 from Prince [3] were considered for this analysis being respectively, the cases with the highest and lowest Mach number. Table 6 and Table 7 additionally present the test conditions considered for the simulations in this analysis.

Since different speed regimes were covered in this part of the study, different meshes were considered. The mesh used for the transonic test case was a hybrid unstructured grid with prismatic embedded layers on the body wall to properly resolve the boundary layer. The baseline mesh used 18 prismatic layers with an average growth ratio of 1.2 and with a first cell spacing designed to give $y^+$ of 3 at x/D=0.01. The outer boundaries for this mesh were located 30 afterbody diameters away from the body at all points, having a hemispherical shape for the inflow followed by a cylindrical section, all of which applied a pressure far field boundary condition to fix the farfield pressure, temperature and Mach number. Following a grid convergence study, a mesh of 2.1 x$10^6$ elements was chosen for the baseline case prior to feature adaption.

In the supersonic cases, the mesh was defined taking as a reference the structured mesh used in Prince [3]. This mesh was also chosen following a mesh sensitivity study, and used 120 cells in each of the I, J, K, computational directions, giving a mesh of 1.73 million elements prior to feature adaption. Here, again, the first cell height above the wall surface was chosen to give a $y^+$ of 3 close to the nose tip. The mesh has a C-topology in the symmetry plane and an O-topology around the body circumference though, like the transonic test case, only a half flow calculation was computed with a symmetry boundary condition on the basis that the experimental flow was known to be symmetric in the plane of windward / leeward flow attachment. The same boundary condition strategy was employed in both cases.

| | |
|---|---|
| **Re** | 1.24x$10^6$ per ft |
| **Mach** | 2.5 |
| **Freestream vel. (m/s)** | 586.31 |
| **P (Pa)** | 8310.928 |
| **T (K)** | 136.888 |
| **AoA (deg)** | 14 |

*Table 6-The supersonic forebody test case conditions.*

| | |
|---|---|
| **Re** | 0.667x$10^6$ per ft |
| **Mach** | 0.7 |
| **Freestream vel. (m/s)** | 229.601 |
| **P (Pa)** | 37108.412 |
| **T (K)** | 267.759 |
| **AoA (deg)** | 14 |

*Table 7-The transonic forebody test case conditions.*

### *4.3.2* Simulation details

A density-based solver was used for the steady simulations in this study considering the compressibility effects present at the experimental conditions. These simulations used a hybrid-type of initialisation and were solved using an explicit formulation for the first 1000 iterations before switching to implicit formulation resulting in a total of 6000 iterations per case. A least Squares Cell-Based spatial discretisation was defined along with first-order equations for the turbulent quantities to reduce computational cost. In Table 8, more details on the chosen solution methods are provided.

| | |
|---|---|
| **Density-based formulation** | Explicit and Implicit |
| **Spatial discretisation - Gradient** | Least squares cell-based |
| **Spatial discretisation – Flux type** | Roe-FDS |
| **Spatial discretisation – Flow (AMG.C)** | Second-order upwind |
| **Spatial discretisation - TKE** | First-order upwind |
| **Spatial discretisation – TDR** | First-order upwind |

*Table 8-Solution methods employed in the forebody calculations.*

Once convergence was obtained in the simulations, a mesh adaption based on pressure gradients was applied and the solutions were then iterated further until convergence was achieved on this refined mesh.

### *4.3.3* Results

Comparisons of the circumferential surface pressure coefficient distribution at different longitudinal

positions are presented. The figures in this section show the results from the different simulation methods mentioned in section 4.3.1 and used data measured at x/D=3.5, 5.5, 7.5, 9.5 and 11.5 for both the transonic (M=0.7 and 14° angle of attack) and the supersonic (2.5 and 14° angle of attack) experiments.

Crossflow total pressure and pitot pressure ratios were obtained respectively for the transonic and supersonic tests by means of a traversing pitot tube, to study the relationship between the local to freestream properties. The measurements were available for the stations at x/D= 8.5 and 11.5 in the transonic case and at x/D=5.5 and 11.5 for the supersonic test and are compared against the simulation data for a qualitative study of the predicted results. Here, the pitot pressure is the local total pressure measured by a pitot tube subjected to supersonic conditions and is obtained with the Rayleigh pitot tube equation:

$$\boldsymbol{P_p = p\left(\frac{(\gamma+1)^2 M^2}{4\gamma M^2 - 2(\gamma-1)}\right)^{\delta/(\delta-1)} \frac{(1-\gamma+2\gamma M^2)}{(\gamma+1)}} \quad (1)$$

Where *M* and *p* are the local values of Mach number and static pressure, respectively, and $\boldsymbol{\gamma}$ is the ratio of specific heats.

Aerodynamic force and moment coefficients were calculated using the afterbody cross-section area as the reference area with the moments being measured about the nose tip. The experimental measurements were only available for the supersonic case at 14° angle of attack and are shown in Figure 18 for the normal and axial forces, and the pitching moment coefficients respectively.

In Figure 14 the comparison between the experimental and computational surface Cp distribution measurements are presented. Here, the results of the RANS turbulence models are presented on the left-hand side for each axial station, while the higher order Reynolds Stress model, as well as the unsteady SAS and DDES methods, are plotted in the right-hand graph for improved clarity. All turbulence methods successfully resolved the pressures on the windward side of the bodies, with differences seen only in the resolution of vortex suction on the leeside of the body. The corresponding comparison of contours of total pressure ratio at the station x/D = 11.5 is presented in Figure 15, where a fully formed primary leeside vortex is resolved by all of the turbulence methods. The combined evidence from figures 14 and 15 reveal that, of the two-equation RANS turbulence models, the K-ε RNG and K-ε Realisable models better predicted the flow topology and surface Cp distribution for this case, while the SAS method was the most accurate out of the high-order methods.

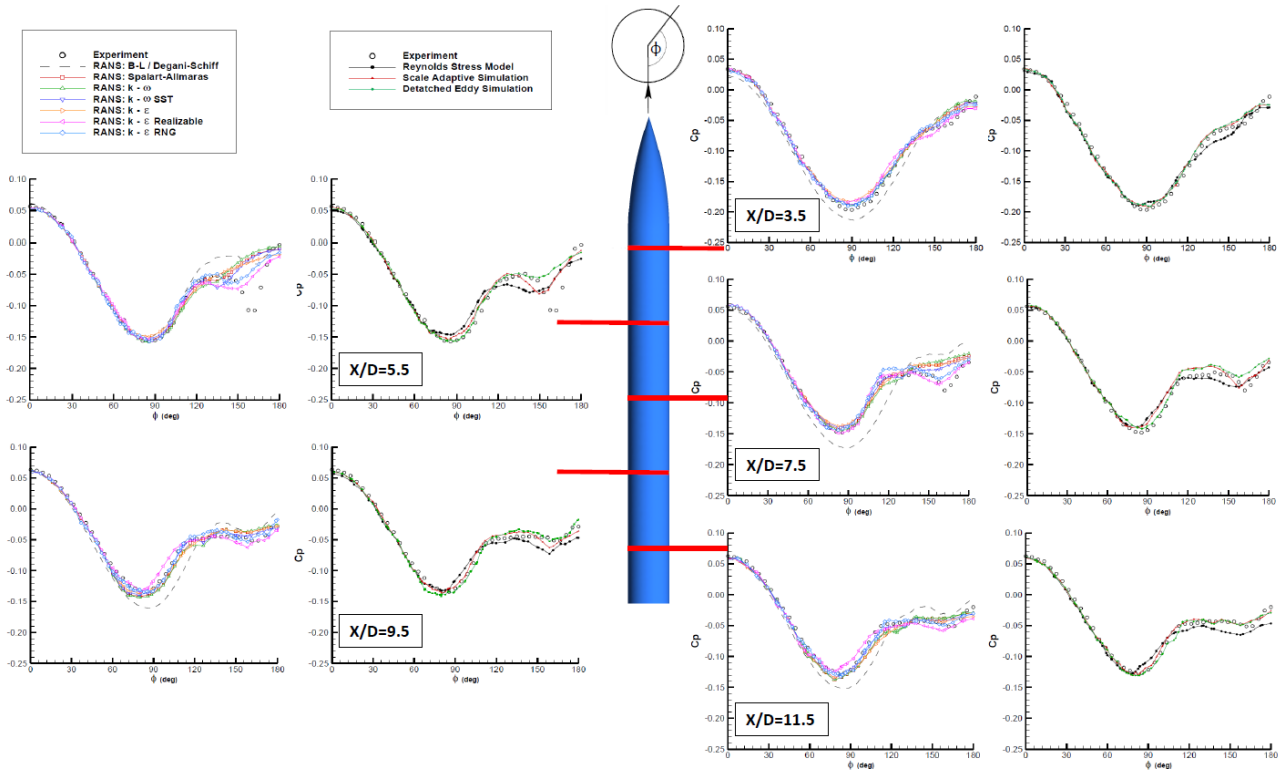


*Figure 14-Circunferential surface Cp distribution, B1A forebody, M=0.7, α=14°.*

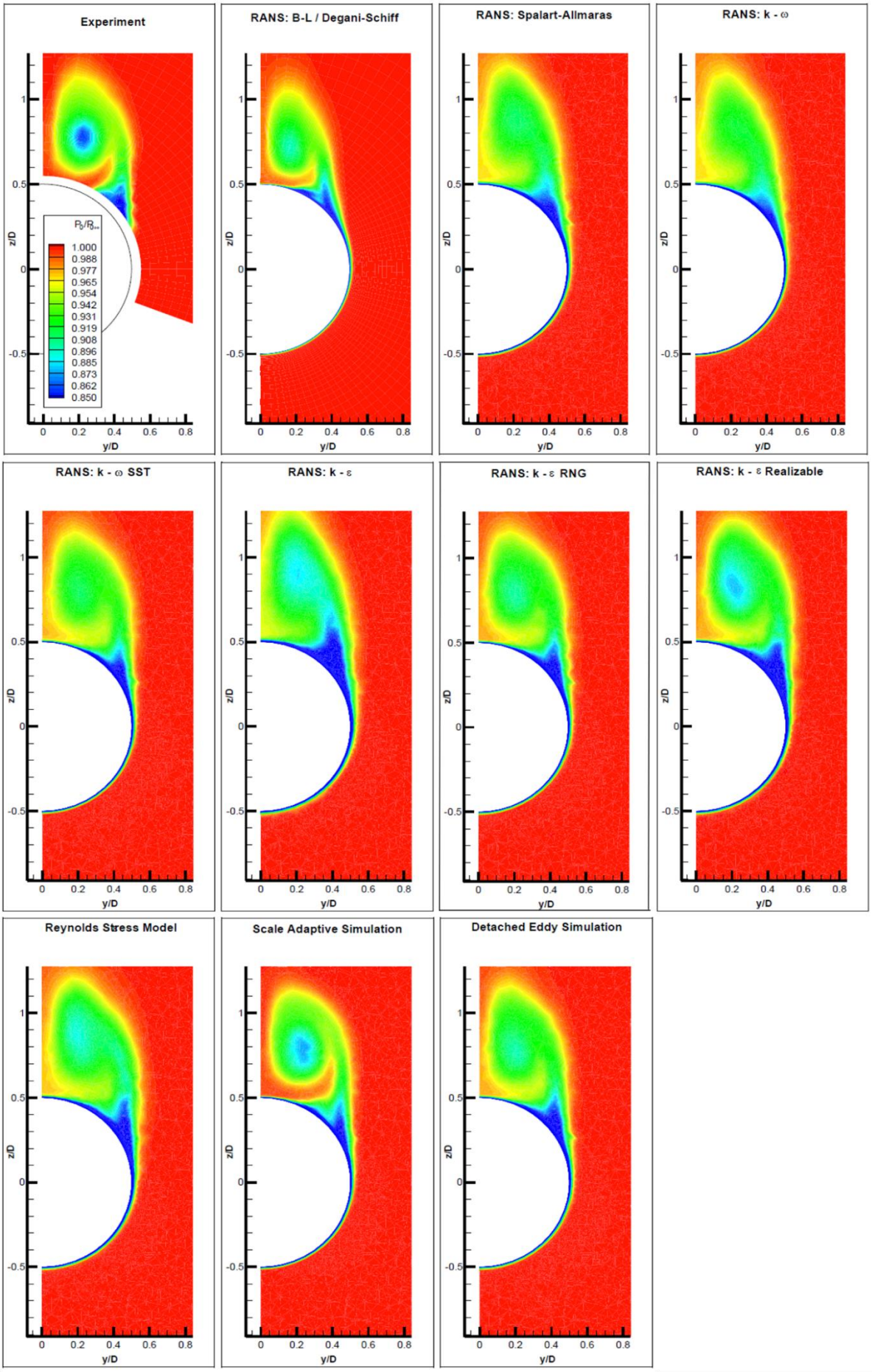


*Figure 15-Total pressure ratio, B1A forebody, M=0.7, α=14°, x/D=11.5.*

The corresponding comparisons for the supersonic flow test case are presented for the surface Cp distribution in Figure 16, and for the pitot-pressure ratio contours in figure 17.

The pressure coefficient distribution showed that only the SAS, *k*-ε Realisable and *k*-ω-SST methods out of the high-order methods and two-equation RANS turbulence models respectively, produced relatively accurate predictions of the primary separation position at the different stations along the body. None of the methods used in this analysis was able to properly predict the extent of the suction produced by the leeward vortices, especially at *x/D* = 7.5 where a second suction peak is predicted implying the existence of a strong secondary vortex that did not appear in the experimental measurements. These differences are, however, more subtle and closer to the experimental reference than the transonic case. Better qualitative comparisons were observed from the pitot pressure ratio contours presented in figure 17 for x/D = 11.5. The main flow features at each station were captured by most of the models, including both the crossflow shockwave at the primary separation location and a secondary vortex beneath the leeside primary system.

The embedded crossflow shockwave formed in a range of circumferential locations between 70° to 120° depending on the longitudinal position, was identified from the sudden pressure jump in the pressure coefficient distribution plots and in the pitot pressure ratio contours. It is seen that most of the models captured a shockwave located at around 5° - 15° further leeward than the one resolved in the experiment surface Cp measurements. Again, the SAS method and the K-ε RNG and K-ε Realisable models provided more accurate predictions of the overall flowfield, including the primary vortex structure and core suction level. In terms of forces and moments, no absolute best turbulence model was identified with most of them showing good correlations in terms of one parameter but less adequate predictions for the other parameters. Overall the K-ε-Realizable and *k*-$\omega$ SST models and the SAS method gave the most accurate predictions of the forces and moments for this case.

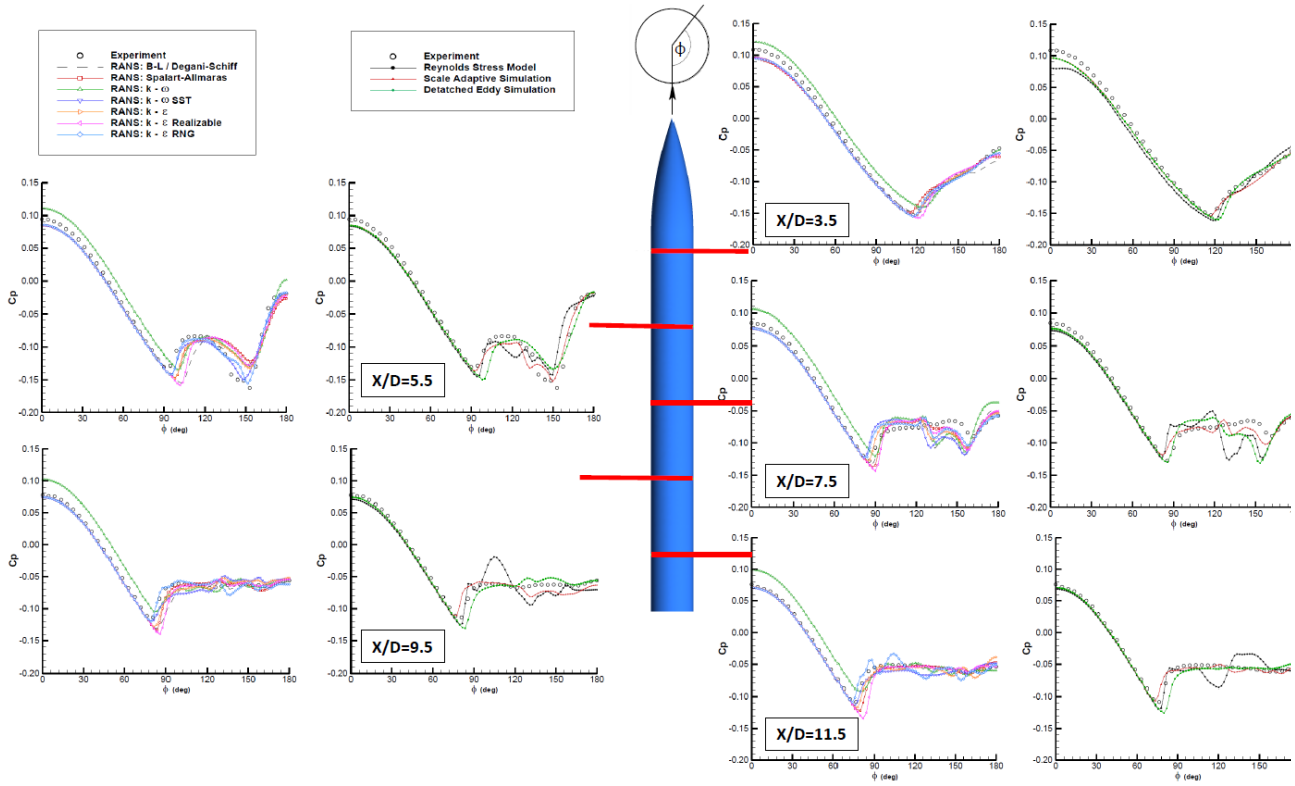


*Figure 16-Circumferential surface Cp distribution, B1A forebody, M=2.5, α=14°.*

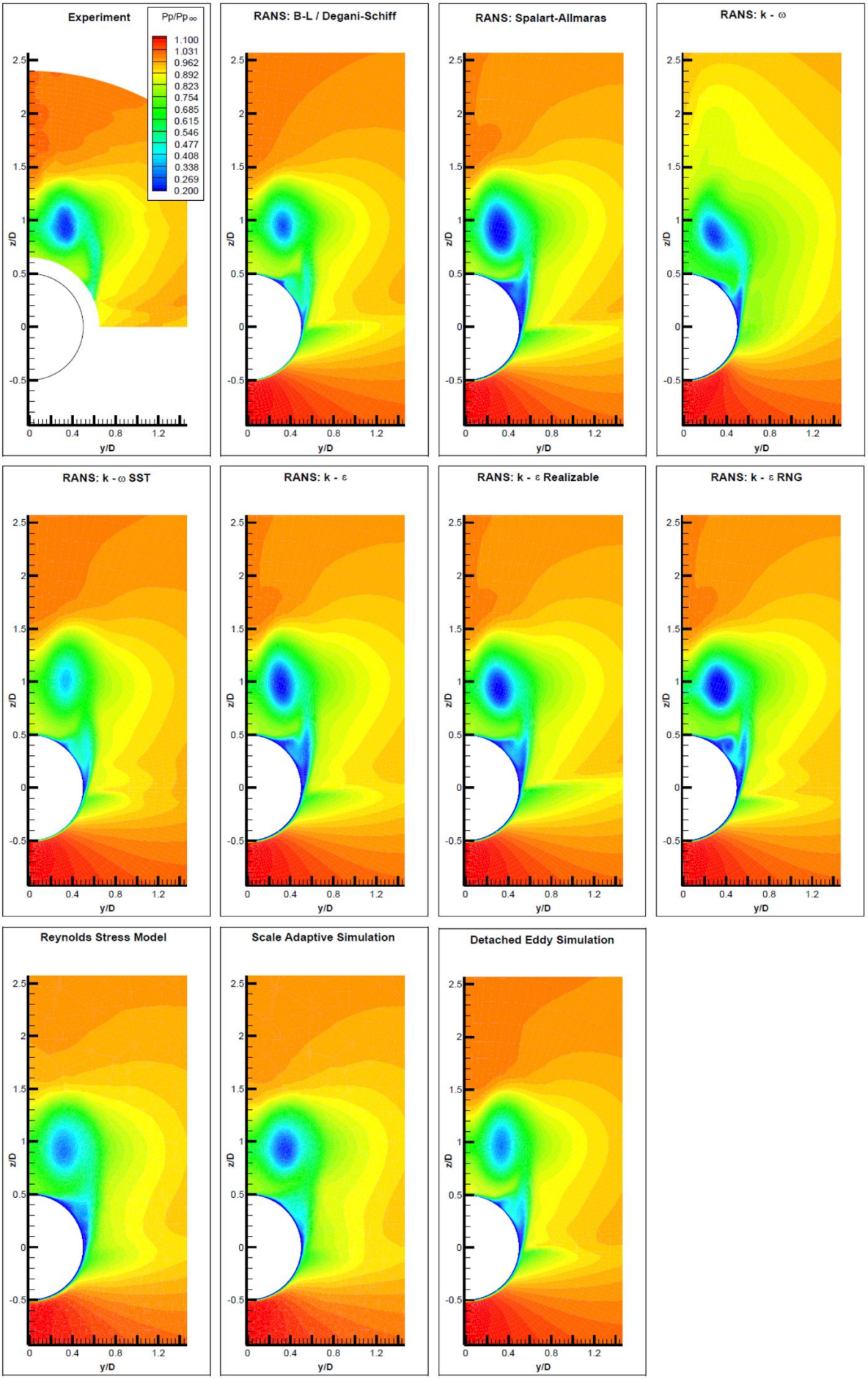


*Figure 17-Pitot pressure ratio, B1A, M=2.5, α=14°, x/D=11.5.*

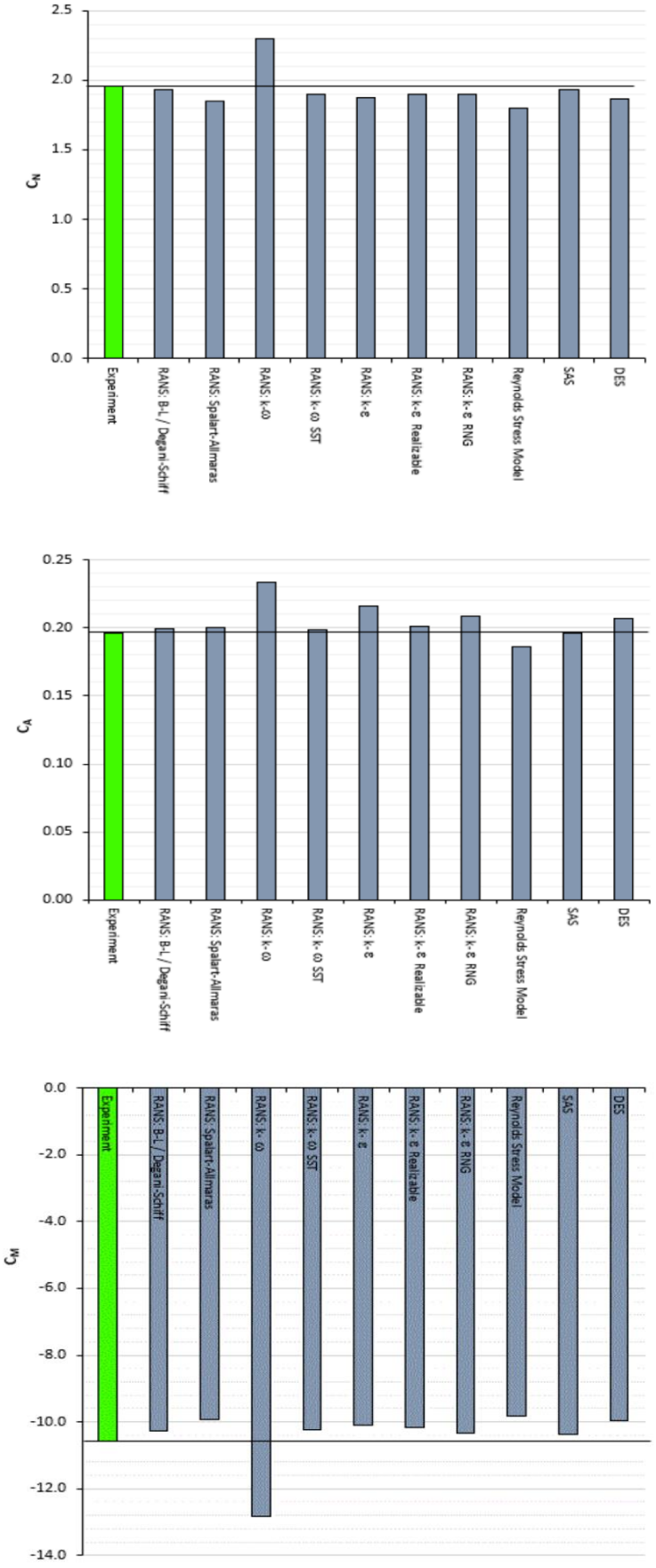


*Figure 18-Aerodynamic forces and moments, B1A forebody, M=2.5, α=14°.*

## 5 Conclusions

The efforts made in the present study allowed to confirm that Reynolds Averaged Navier-Stokes methods can successfully model the overall flow structure for cases at low and high speed. Besides, the models can capture vortical flows around delta wings and cylindrical forebodies, predict the forces and moments to within 10-15% of those measured in the experimental references, and successfully resolve the overall trends with Mach number and angle of attack. However, the turbulence models cannot resolve the finer flow details, such as the magnitude of vortex suction or the features of the secondary vortex formed in some of the tested cases.

The validation studies also showed no universal method for the computational prediction of turbulent vortical flows. However, it allowed to identify the Scale Adaptive Simulation method as the one that provides the most accurate predictions of the steady vortex flows at low to moderate angles of attack. Similarly, the k-ε Realisable and k-ω SST turbulence models were the ones that provided the closest predictions out of the Reynolds Averaging linear eddy viscosity models.

For the purposes of design studies, where highly accurate flow simulations are not required and where aerodynamic characteristics within 10% of measured data are acceptable, RANS based predictions are capable of providing adequate trend predictions. However, where more detailed flow physics studies are required, particularly if flow unsteadiness needs to resolve, higher fidelity methods such as Delayed Detached Eddy Simulation or Large Eddy Simulation must be employed on extremely fine meshes. The study performed a series of unsteady DDES as a first approach to the method. More efforts are required to define the suitable time resolution and assure the mesh resolution is adequate for an in-depth descriptive analysis of the phenomena.

## Copyright Statement



## References

[1] J. Rech, C. Leyman, “Concorde aerodynamics and associated systems development”, AIAA professional study series, New York, 1980

[2] “Space shuttle aerothermodynamics technology conference”, NASA TM X-2508,1972

[3] S. A. Prince, The aerodynamics of high speed aerial weapons, Cranfield University, PhD thesis, 1999

[4] D. Hummel, “Experimental investigation of the flow on the suction side of a thin delta wing, NASA TM-75897,” no. March 1981, 1981.

[5] N. C. Lambourne and D. W. Bryer. Some measurements in the vortex flow generated by a sharp leading edge having 65° sweep,ARC CP 477 (1959).

[6] H. Werlé, “Sur l'eclatement des tourbillons d'apex d'une aile delta aux faibles vitesses”, La Recherche Aeronautique, No. 74. pp. 23 to 30. January- February, 1960.

[7] S. O. Kjelgaard and W. L. Sellers III, “Detailed Flow-Field Measurements Over a 75° Swept Delta Wing”, NASA-TP-2997,1990.

[8] Stanbrook A, and Squire L. Possible types of ow at swept leading edges. The Aeronautical Quarterly. 1964;15(1):72:82.

[9] D. S. Miller and R. M. Wood, Lee-Side Flow Over Delta Wings at Supersonic Speeds NASA TP-2430, June 1985

[10] Lambourne, N. C.; and Bryer, D. W.: “The Bursting of Leading-Edge Vortices—Some Observations and Discussion of the Phenomenon”. R. & M. No. 3282, British Aeronautical Research Council, Apr. 1961.

[11]Escudier, M., “Vortex Breakdown: Observations and Explanations”, Progress in Aerospace Sciences, Vol. 25, pp. 189-229, 1988.

[12]Delery, J., “Aspects of Vortex Breakdown,” Progress in Aerospace Sciences, Vol. 30, p. I-59, 1994.

[13]J. M. Luckring, D. Hummel, “What was learned from the new VFE-2 experiments?”, *Aerosp. Sci. Technol.*, vol. 24, no. 1, pp. 77–88, 2013.

[14]V. M. L. Edge, J. Chu, and J. M. Luckring, “Experimental Surface Pressure Data Obtained on 65 ° Delta Wing Across Reynolds Number and Mach Number Ranges, Volume 3 – Medium Radius Leading Edge” *Nasa Tech. Memo. 4645*, . February, 1996.

[15]J. M. Luckring, “Reynolds Number and Leading-Edge Bluntness Effects on a 65 ° Delta Wing,” *40th AIAA Aerosp. Sci. Meet. Exhib.*, AIAA Paper 2002-0419. January, 2002.

[16]F. N. Coton, S. Mat, R. A. M. D. Galbraith, and R. Gilmour, “The effect of leading edge radius on a 65° delta wing,” *47th AIAA Aerosp. Sci. Meet.* AIAA Paper 2009-1293, January 2009.

[17] A. R. Rao, B. Nath, N. Gopinath, and K. R. R. D, “Reynolds Number and Leading Edge Bluntness Effects on 65 ° Delta Wing At Subsonic Speed,” in *Symposium on Applied Aerodynamics and Design of Aerospace Vehicle (SAROD 2011)*, 2011, Bangalore, India

[18] J. T. Kegelman and F. W. Roos, “Effects of leading edge shape and vortex burst on the flowfield of a 70-degree-sweep delta wing”, AIAA Paper No. 89-86, 1989.

[19]Olsen, P., and Nelson, R., “Vortex Interaction over Double-Delta Wings at High Angles of Attack,” AIAA Paper 89-2191, July/Aug. 1989.

[20]N. G. Verhaagen, “Effects of Reynolds number on flow over 76/40 degree double delta wing”, Journal of aircraft, Vol. 39, No. 6, pp. 1045–1052. 2002

[21]N. G. Verhaagen, L. N. Jenkins, S. B. Kern and A. E. Washburn, “A study of the vortex flow over a 76/40-deg double-delta wing”, AIAA Paper 95-0650, Nevada, 1995

[22]S. B. Kern, Vortex flow control using fillets on a double-delta wing, Journal of aircraft, Vol. 30, No. 6, pp. 818–825, 1993

[23]G. E. Erickson and H. A. Gonzalez, Wind tunnel application of a pressure sensitive paint technique to a Double Delta Wing Model at Subsonic and Transonic Speeds, NASA TM 2006-214319., 2006.

[24]S. K. Hebbar et al., Experimental study of vortex flow control on double-delta wings using fillets, Journal of aircraft, Vol. 33, No. 4, pp. 743–751, 1996

[25]U. Brennenstuhl and D. Hummel, “Vortex Formation Over Double-Delta Wings.,” *Congress of the International Council of the Aeronautical Sciences*, vol. 2. pp. 1133–1146, 1982.

[26]S. L. Gai, M. Roberts, A. Barker, C. Kleczaj, and A. J. Riley, “Vortex interaction and breakdown over double-delta wings,” *Aeronaut. J.*, vol. 108, no. 1079, pp. 27–34, 2004

[27] J. Rom, *High angle of attack aerodynamics*. Springer-Verlag, 1992.

[28] Ward, L. C. Pressure Measurements on an Axisymmetric Body at Mach Numbers from 2.5 to 4.5, RAE TM Aero 2174,1990

[29] Wardlaw, A. B. “High Angle of Attack Missile Aerodynamics” AGARD Lecture Series (Missile Aerodynamics), 1979.

[30]H. K. Versteeg and W. Malalasekera, *An Introduction to Computational Fluid Dynamics*, 2nd ed. Pearson Education, 2007.

[31]J. M. Luckring, “The discovery and prediction of vortex flow aerodynamics”, The Aeronautical Journal, Vol. 123 No. 1264, pp 729-804, April 2019

[32]P. Moin and K. Mahesh, Direct numerical simulation: A tool in turbulence research, Center for Turbulence Research, Stanford University, Annual Review of Fluid Mechanics, vol. 30:539–78, 1998

[33]D. McLean, *Understanding Aerodynamics, arguing from the real physics*. Wiley, 2013.

[34] T. Nishino, G. T. Roberts, and X. Zhang, “Unsteady RANS and detached-eddy simulations of flow around a circular cylinder in ground effect,” *J. Fluids Struct.*, vol. 24, no. 1, pp. 18–33, 2008.

[35] L. Davidson, “Fluid mechanics, turbulent flow and turbulence modeling,” *CFD course, Division of fluid Dynamics, Chalmers University of Technology*. Division of fluid dynamics, Chalmers University of Technology, pp. 1–270, 2020.

[36] P. R. Spalart, S. Deck, M. L. Shur, K. D. Squires, M. K. Strelets, and A. Travin, “A new version of detached-eddy simulation, resistant to ambiguous grid densities,” *Theor. Comput. Fluid Dyn.*, vol. 20, no. 3, pp. 181–195, 2006.

[37] F. R. Menter and Y. Egorov, “The scale-adaptive simulation method for unsteady turbulent flow predictions. part 1: Theory and model description,” vol. 85, no. 1, pp. 113–138, 2010.

[38]F. R. Menter, M. Kuntz, and R. Bender, “A Scale-Adaptive Simulation Model for Turbulent Flow Predictions, AIAA 2003-0767,” in 41st Aerospace Sciences Meeting and Exhibit, 2003, no. January.

[39] A. F. T. Guide, “Ansys Fluent Theory Guide,” *ANSYS Inc., USA*, vol. 15317, no. November, pp. 724–746, 2013.

[40]G. Eggenspieler, “Modelling Laminar-Turbulent Transition Processes,” *ANSYS Inc.* p. 25, 2012.

[41]S.A. Prince, N. Qin, “Mechanisms of windward vortex shocks about supersonic slender bodies”, Royal Aeronautical Journal, Vol 106, no. 1063, September 2002.